# Screw rotor manufacturing via 5-axis flank CNC machining using conical tools

Michal Bizzarri[*,a,c], Pengbo Bo[b], Michael Bartoň[c,d]

[a] *Department of Mathematics, Faculty of Applied Sciences, University of West Bohemia, Univerzitní 8, 301 00 Plzeň, Czech Republic*
[b] *School of Computer Science and Technology, Harbin Institute of Technology, West Wenhua Street 2, 264209 Weihai, China*
[c] *BCAM – Basque Center for Applied Mathematics, Alameda de Mazarredo 14, 48009 Bilbao, Basque Country, Spain*
[d] *Ikerbasque – Basque Foundation for Sciences, Maria Diaz de Haro 3, 48013 Bilbao, Basque Country, Spain*

**Abstract**

We propose a new method for 5-axis flank computer numerically controlled (CNC) machining of screw rotors using conical tools. The flanks of screw rotors consist of helical surfaces, which predetermines the motion of the milling tool and reduces the search space for tool positioning to only 4-parametric family, which allows a quick search for good initial positions of a given conical tool. We initialize the search by looking at second order line contact between the tool and the helical flank of the rotor. Several positions of the tool are found, covering major part of the flank of the rotor, followed by global optimization that further reduces the tool-surface error and makes sure that there are no gaps between neighboring sweeps of the tool. We demonstrate our approach on several benchmark screw rotors, showing that our approach meets fine industrial tolerances with only few sweeps of the tool.

*Key words:* 5-axis CNC machining, flank milling, conical tool, screw rotor

## 1. Introduction and motivation

Inspired by industrial needs, efficient and highly accurate manufacturing of free-form objects has been of interest for several decades [1–6]. Computer numerically controlled (CNC) machining is the leading subtractive manufacturing technology and even though nowadays additive manufacturing is increasing its share on the manufacturing market [7], certain types of mechanical components like turbine blades or engine components are, due to the stiffness requirements, preferred to be manufactured from a single material block.

One such an object is a *screw compressor*, that is a two-piece gas/fluid transition mechanism, consisting of two screw components, two parallel helical rotors, a *male rotor* and a *female rotor*, which are engaged one with the other as they rotate, cf. Fig. 1 (a). The fluid captured in the cavity between the two parts moves in a direction of the two parallel axes as the mechanism rotates. The geometry of screw rotors may vary depending on the number of *lobes* in each rotor, the basic *rotor profile*, and relative proportions of each rotor lobe segment, however, geometrically the boundaries of screw rotors are always helical surfaces. Highly accurate manufacturing of screw rotors is essential as it increases lifespan of the mechanism as well as it affects the quality of gas/fluid transition.

Our work aims at the final stage of the manufacturing process, called *flank milling* where the milling tool moves tangentially along the to-be-manufactured surface, and is therefore required to be in a tangential configuration not only at a single point, but along a whole 3D curve. It has been shown recently that screw rotors can be well approximated by helical motions of a custom-shaped tool such that the tool touches

[*] Corresponding author
*Email addresses:* bizzarri@kma.zcu.cz (Michal Bizzarri), pbbo@hit.edu.cn (Pengbo Bo), mbarton@bcamath.org (Michael Bartoň)

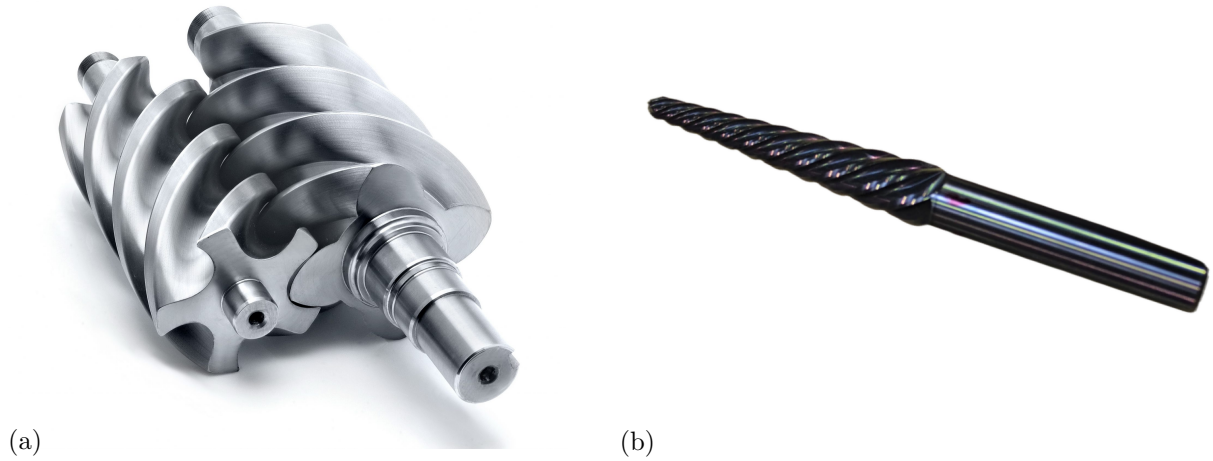

(a) (b)

Figure 1: (a) A screw rotor consisting of a female and a male part. (b) A typical conical tool for flank milling. The tool contains several flutes, but under high spin it can be conceptualized as a truncated cone.

simultaneously both flanks of the rotor, resulting in *double-flank* milling [8]. However, such an approach requires a special, *custom-shaped*, tool that has to be designed, and manufactured, for each particular rotor individually. In contrast, we propose a path-planning algorithm for a given on-market tool. While we demonstrate our algorithm on the case study of screw rotors, the proposed approach is general for an arbitrary helical surface.

Our research focuses on traditional, on-market tools, that for flank milling are typically conical or cylindrical. In such a case, double-flank milling is not possible, however, even highly accurate (single-) flank milling is of interest without the need of a special tool.

Given a helical surface, the goal of this paper is to find, for a given conical tool $T$, a family of its milling paths $C_i$ such that the paths approximate the helical surface within fine machining tolerances (several micrometers), and the helical surface can be flank-milled by a *single* conical tool.

Our main contributions contain:

- Local cutter-workpiece analysis and cutter selection (Section 4).
- Global optimization of the cutter-tool error (Sections 5.2 and 5.4), including the search for the optimal conical cutting tool (Section 5.3).
- Comparison against [8], which is a theoretically exact method for symmetrical profiles, however, it requires an expensive custom-shaped tool.

The rest of the paper is organized as follows. Section 2 surveys the state of the art on design and manufacturing of screw rotors and Section 3 briefly discusses preliminaries on helical and conical surfaces, and introduces the notion of envelope in the context of 5-axis CNC machining. Section 4 discusses the cutter selection from the point of view of approximation quality and gives bounds on the tool parameters in order to match the rotor geometry. Section 5 describes the three main optimization algorithms and Section 6 shows several examples on benchmark rotors. Finally, Section 7 draws a few directions for future research and concludes the paper.

## 2. Previous work

Design and manufacturing of screw rotors is a well studied problem that has been investigated for decades [9–12] and the theoretical grounds for good approximation of a helical surface by an envelope of a cone/cylinder locally, close to a single contact point, have been laid down decades ago [13].

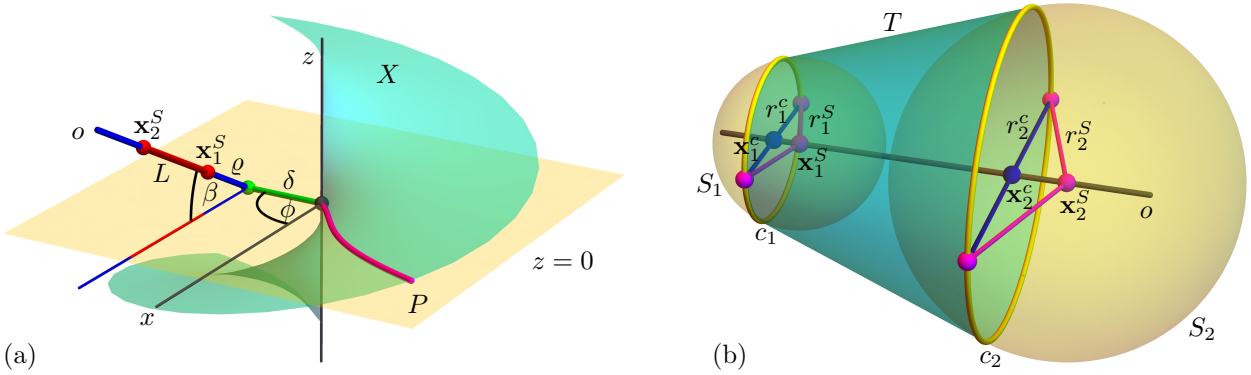


Figure 2: (a) Helical surface $X$ obtained by screwing the planar profile $P$ and a generic position of the axis $o$ determined by the values $(\delta, \beta, \phi)$. The corresponding line segment $\mathbf{x}_1^S, \mathbf{x}_2^S$ of the axis is then given by parameters $\varrho$ and $L$. (b) Truncated cone $T$ given by the centers $\mathbf{x}_i^S$ and radii $r_i^S$ of its boundary inscribed spheres $S_i$, $i = 1, 2$.

Since matching of the screw rotors can be conceptualized in the 2D plane perpendicular to the rotor axis, many matching principles from the gear theory can be applied to rotors too [11, 14–16]. Explicit formulae for the female rotor using analytic functions are given in [17]. The profile consists of straight lines, circular and elliptical arcs, and trochoids, that depend on several parameters. These parameters in the analytic expression are further optimized using sequential unconstrained minimization method and physical experiments are conducted to validate the performance of the designed rotor.

An alternative approach for the rotor design is proposed in [18] where one starts with so called *meshing line*, a locus of points along which the rotors touch in time, and computes the two profiles accordingly.

Manufacturing of screw rotors is typically realized using special machine tools via hobbing and/or grinding [19]. An alternative manufacturing process is resin transfer molding (RTM) that uses a separable four-piece mold [20], and the rotors are manufactured from composite materials consisting of chopped carbon fibers.

There are other physical factors that affect performance of the rotor like the temperature, the type of fluid or gas that is being transferred, or the type of operation mode (oil-free or oil-lubricated), see e.g. [21] and the references cited therein. In our work, we focus solely on the geometric aspects of rotor quality, i.e., the approximation error between the designed shape and its approximation using a set of motions of a conical tool.

## 3. Preliminaries

We now briefly recall basic notions of helical surfaces, conical milling tools, and basic principles of flank milling.

### *3.1. Helical surfaces*

The helical surface $X$ is obtained by a helical motion on the planar profile $P$. The helical motion is defined by its *axis*, w.l.o.g. we identify it with the axis $z$, *handedness* (it can be right-handed (+) or left-handed (-)) and the value of *pitch* $2\pi v_0$, see Fig. 2 (a) Therefore, the right/left movement of the screw in time $t$ is given as follows:

$$S^{\pm}_{t,z,v_0} \circ (p_x, p_y, p_z) = (p_x \cos t \mp p_y \sin t, p_x \sin t \pm p_y \cos t, t\, v_0 + p_z). \tag{1}$$

The profile $P$ to define the shape of $X$ typically lies in a plane perpendicular to the screw axis, $z = 0$ in Fig. 2 (a). Another option is for $P$ to lie in a plane that contains the axis. In such a case, we speak about a

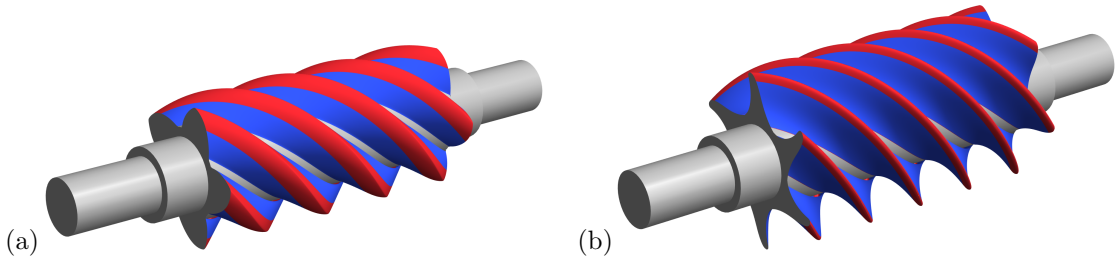


Figure 3: The helical flanks of male (a) and female (b) screw rotors are color-coded by the Gaussian curvature $K$. The elliptic (hyperbolic) points with the positive (negative) Gaussian curvature are shown in red (blue).

*meridian*. The helical surface can of course be defined by any other curve (different from the corresponding helices), see later Remark 4.2 on another convenient choice.

The shape of $X$, in terms of Gaussian curvature $K$, depends on the shape of $P$, that is, a helical surface can contain all three types of points: elliptic ($K > 0$), parabolic ($K = 0$), and hyperbolic ($K < 0$). Since we are interested in approximation of $X$ by an envelope of a cone, highly accurate approximation is possible only in the parts where $K < 0$. One can see that the female rotor consists of mainly hyperbolic points while for the male part only the part of lobes closer to the axis meets this criterion, see Fig. 3.

### *3.2. Conical tools*

The most commonly used tools for flank milling are conical tools, see Fig. 1 (b). To be precise, these tools are provided by teeth/flutes that serve for material removal, so their meridians are not exactly straight lines. However, assuming a much higher rotational speed of the tool about its axis compared to the motion of the axis, these tools are usually considered as truncated cones for geometric modelling and path planning purposes.

Consider a truncated cone $T$ given by the centers $\mathbf{x}_i^c$ and radii $r_i^c$ of its boundary circles $c_i$, $i = 1, 2$, see Fig. 2 (b). The inscribed spheres $S_i$ touching $T$ along $c_i$ have centers and radii

$$\mathbf{x}_i^S = \mathbf{x}_i^c + r_i^c \tan\alpha\, \mathbf{a}, \qquad r_i^S = \frac{r_i^c}{\cos\alpha}, \tag{2}$$

where $\alpha$ is the so called *opening angle*

$$\alpha = \arctan\left(\frac{r_2^c - r_1^c}{\|\mathbf{x}_2^c - \mathbf{x}_1^c\|}\right) = \arcsin\left(\frac{r_2^S - r_1^S}{\|\mathbf{x}_2^S - \mathbf{x}_1^S\|}\right) \tag{3}$$

and $\mathbf{a}$ is the unit vector in the direction of the tool's axis $o$, i.e.,

$$\mathbf{a} = \frac{\mathbf{x}_2^c - \mathbf{x}_1^c}{\|\mathbf{x}_2^c - \mathbf{x}_1^c\|} = \frac{\mathbf{x}_2^S - \mathbf{x}_1^S}{\|\mathbf{x}_2^S - \mathbf{x}_1^S\|}. \tag{4}$$

The "$c$" terms relate $\alpha$ and $\mathbf{a}$ to the centers and radii of the *circles*, while the "$S$" terms give an equivalent expression with respect to the *sphere* centers and radii, see Fig. 2 (b). We define the tool's length $h$ as the distance of the boundary circles' centers

$$h = \|\mathbf{x}_2^c - \mathbf{x}_1^c\|, \tag{5}$$

whereas the distance between the centers $\mathbf{x}_i^S$ of the boundary spheres is denoted by $L$, i.e.,

$$L = \|\mathbf{x}_2^S - \mathbf{x}_1^S\|. \tag{6}$$

The lengths $h$ and $L$ are related as follows:

$$L = h + (r_2^c - r_1^c)\tan\alpha = h + (r_2^S - r_1^S)\sin\alpha. \tag{7}$$

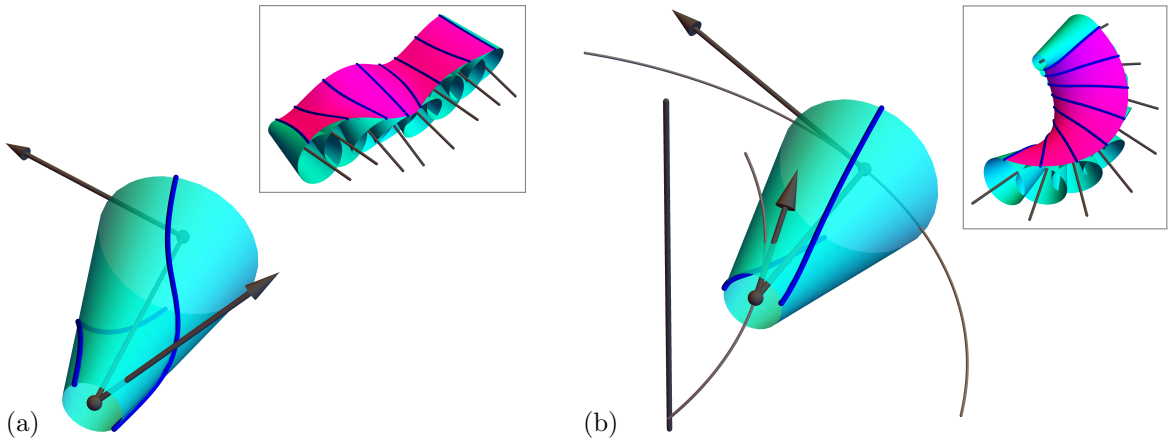


Figure 4: Envelope of a moving truncated cone. General characteristic (blue curve) depends on the instantaneous motion and therefore changes dynamically in time (a). For a helical motion, this curve is constant in time (b).

The shape of the truncated cone is determined by a triplet of independent parameters; we select the opening angle and the radii of the boundary circles, i.e., $(\alpha, r_1^c, r_2^c)$.

Further, we employ the following generic parametrization of the particular segment of length $L$ of the axis $o$ of $T$

$$\begin{aligned}\mathbf{o}(s) &= R_{\phi,z} \circ ((\delta, 0, 0) + (\varrho + Ls)\,(0, \cos\beta, \sin\beta)) \\ &= (\delta\cos\phi - (\varrho + Ls)\cos\beta\sin\phi, (\varrho + Ls)\cos\beta\cos\phi + \delta\sin\phi, (\varrho + Ls)\sin\beta)\,, \quad s \in [0,1], \end{aligned} \tag{8}$$

where $\beta$ is the angle between $o$ and the plane $z = 0$, $\phi$ is the angle that controls the rotation of $o$ around the $z$-axis, $\delta$ is the distance of $o$ and the $z$-axis and $\varrho$ is the distance between $\mathbf{x}_1^S = \mathbf{o}(0)$ and the intersection of $o$ with the plane $z = 0$, see Fig. 2 (a). Finally, we employ the corresponding radial function describing the radii of the spheres inscribed into $T$

$$r(s) = (1 - s)r_1^S + s\, r_2^S, \quad s \in [0, 1]. \tag{9}$$

Using parameterization of the tool axis (8) and radial function (9), we have

$$\mathbf{x}_1^S = \mathbf{o}(0), \quad \mathbf{x}_2^S = \mathbf{o}(1), \quad r_1^S = r(0), \quad r_2^S = r(1). \tag{10}$$

### *3.3. Flank milling*

Flank (aka side) milling is typically used as a final stage of the manufacturing process where the milling tool moves tangentially along the reference geometry. Geometrically, flank milling can be interpreted as an approximation problem that takes the reference surface $X$ and approximates it by an *envelope* of a moving tool $T$. The tool touches the envelope along a 3D curve $\mathbf{ch}$, called *characteristic*. This curve is in general not static; its shape depends on the instantaneous motion of the tool and therefore changes in time as the instantaneous motion changes, see Fig. 4 (a). For screw motions, however, the characteristic is constant in time, see Fig. 4 (b). For a moving (infinite) cone, the characteristic is an algebraic curve of degree four that passes through the cones' vertex [22]. For a truncated cone it is its corresponding segment.

Applying screw motion (1) to the tool axis (8) we obtain medial surface $\mathbf{y}(s, t)$ which together with radial function (9) yields the *Medial Axis Transform* $(\mathbf{y}(s, t), r(s))$ describing all the spheres inscribed into $T$ in

time. Then using the envelope formula [23] to $\mathbf{y}(s,t)$ and $r(s)$ we obtain the following parameterization of the envelope surface

$$\mathbf{x}^{\pm} = \mathbf{y} - r\,\frac{r'(G\mathbf{y}_s - F\mathbf{y}_t) \pm (\mathbf{y}_s \times \mathbf{y}_t)\sqrt{(E - r'^2)G - F^2}}{EG - F^2}, \tag{11}$$

where $y_s$ and $y_t$ denote the partial derivative of $y$ with respect to $s$ and $t$, respectively, and $E, F, G$ are the components of the first fundamental form of $\mathbf{y}(s,t)$. In our specific setting and for right-handed screw motion (which corresponds to our testing surfaces from Section 6), we have

$$\begin{aligned}\mathbf{y}(s,t) = (&\cos s(\delta\cos\phi) - \cos\beta\sin\phi(\varrho + Lt)) - \sin s(\cos(\beta)\cos\phi(\varrho + Lt) + \delta\sin\phi),\\ &\cos s(\cos\beta\cos\phi(\varrho + Lt) + \delta\sin\phi) + \sin s(\delta\cos\phi - \cos\beta\sin\phi(\varrho + Lt)), \sin\beta(\varrho + Lt) + sv_0)\,.\end{aligned} \tag{12}$$

Since the characteristic in screw motion is constant in time we can, w.l.o.g, set $t = 0$ and then $\mathbf{x}^{\pm}(s,0)$ describes the characteristic where

$$\begin{aligned}\mathbf{y}_t &= (-L\cos\beta\sin\phi, L\cos\beta\cos\phi, L\sin\beta)\,;\\ \mathbf{y}_s(s) &= (-(\cos\beta\cos\phi(\varrho + Ls)) - \delta\sin\phi, \delta\cos\phi - \cos\beta\sin\phi(\varrho + Ls), v_0)\,;\\ r' &= r_2^S - r_1^S\end{aligned} \tag{13}$$

and

$$\begin{aligned}E &= L^2;\\ F &= L(\delta\cos\beta + v_0\sin\beta);\\ G(s) &= \cos^2\beta(\varrho + Ls)^2 + \delta^2 + v_0^2.\end{aligned} \tag{14}$$

In general, there are two branches of the envelope, the *upper* envelope $\mathbf{x}^+$ and the *lower* envelope $\mathbf{x}^-$. As our motivation is the CNC application, we are interested only in that branch that is closer to the the reference surface $X$. Therefore, if there is no danger of confusion, we omit the superscript and write only $\mathbf{x}$, which is assumed to be the desired branch.

For a general motion of a cone, its envelope is a surface with non-positive Gaussian curvature. The vanishing Gaussian curvature occurs in situations with trivial instantaneous motions as translations or rotations, where the characteristic can be a ruling of the cone, which results in a (developable) ruled surface as the envelope. Excluding these motions from our considerations, for a helical instantaneous motion, at every real[1] point of the characteristic, there is a ruling contained inside the envelope which implies the point's hyperbolic nature as a point of the envelope. Consequently flank milling using conical tools can be highly accurate only for hyperbolic surfaces.

## 4. Local analysis and cutter selection

Given a hyperbolic helical surface $X$, we aim to find a conical cutting tool $T$ that can be used for flank milling of $X$. For flank milling, $X$ and $T$ have to be in good alignment along a whole curve (characteristic) hence a necessary condition is a good local alignment at a single point. Therefore, we start our discussion locally, at a specific contact point $\mathbf{q}$, $\mathbf{q} \in X \cap T$. We aim at second order contact of $X$ and $T$ in a certain tangent direction $\mathbf{d}$, so called *second order line contact*, see [24] for more details. It is well known that this contact corresponds to a tangential contact between the Dupin indicatrix of the tool, $i_T$, and the surface, $i_X$, at $\mathbf{q}$, see Fig. 5 (a). Let us emphasize that points on different circles of $T$ possess different curvatures – for the sake of symmetry, we consider a point $\mathbf{q}$ on the middle circle of $T$. Due to the helical nature of $X$, it is sufficient to perform this local contact analysis along a single curve, e.g., a profile curve $P$ of $X$. Such an analysis gives a one-parameter family of constraints on the tool orientations. We also use this analysis to derive the necessary conditions on second order line contact and estimate the size and shape of admissible conical tools.

[1] For certain positions of the cone w.r.t the helical axis, the characteristic can have only complex points.

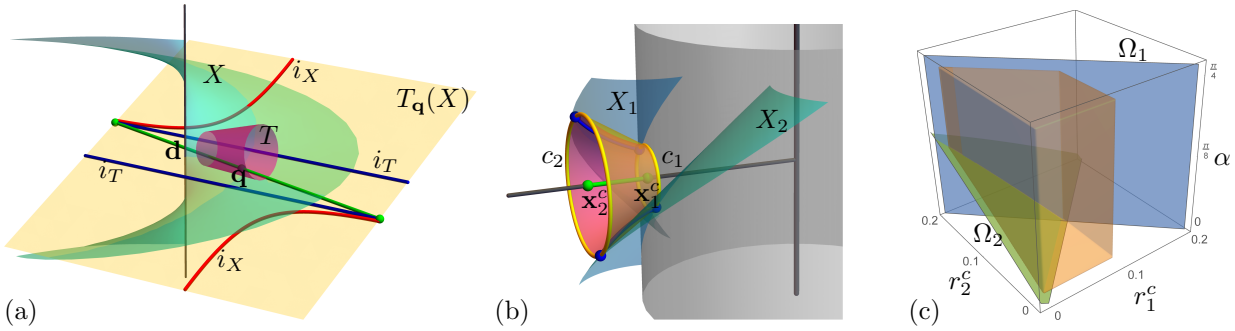


Figure 5: (a) A line contact of $X$ and $T$ at point $\mathbf{q}$. In the common tangent plane $T_{\mathbf{q}}(X)$, the Dupin indicatrices of $X$, $i_X$, and $T$, $i_T$, touch along a common diameter (green) in the direction $\mathbf{d}$. In this common tangent direction, $X$ and $T$ match up to second order. (b) Custom-shaped tool (magenta), designed by the method [8] for the double-flank milling of $X = X_1 \cup X_2$, corresponds to the maximal tool which can be placed into the rotor valley. The boundary circles $c_1$ and $c_2$ define a truncated cone (yellow) which restrict our search space for a conical tool. (c) A subset of the $(r_1^c, r_2^c, \alpha)$-space corresponding to the possible conical tools of the male rotor from Example 6.1.

### *4.1. Necessary local conditions for second order line contact*

We consider only hyperbolic parts of $X$ here, so the Dupin indicatrix is a hyperbola. The Dupin indicatrix of $T$ is a pair of straight lines, whose distance depends on the shape of the conical tool and a position of the contact point. Therefore, second order line contact between $X$ and $T$ at $\mathbf{q}$ is possible if and only if a pair of lines can touch the hyperbola, see Fig. 5 (a). The case of the elliptic parts of $X$ is discussed later in Section 6.1.

**Remark 4.1.** Note that the Dupin indicatrix is typically a pair conic sections, the intersections of the osculating paraboloid with a pair of planes parallel to the tangent plane at the point of interest. At a hyperbolic point, for example, the Dupin indicatrix is a pair of hyperbolas. However, as we are interested in CNC machining applications, we speak about the Dupin indicatrix as a single conic section; again, the one that is related to the surface from the machining side.

We discretize the profile curve $P$ of $X$ by a set of points $\mathbf{q}_1, \ldots, \mathbf{q}_n$, uniformly arc-length distributed samples, at which the Dupin indicatrices are hyperbolas $H_1, \ldots, H_n$. Let us denote by $a_i$ and $b_i$ the lengths of the hyperbola's major and minor semi-axis, respectively, $i = 1, \ldots, n$.

**Remark 4.2.** The profile curve $P$ is just a particular instance of a curve defining the helical surface $X$ and any other curve on $X$ can be used instead. In particular using and sampling an orthogonal trajectory of the helical paths provides more uniform distribution of the points on $X$.

Then the principal curvature radii of the tool at the boundary points, i.e., points of the boundary of the truncated cone, are

$$\left(\infty, r_1^S\right) \quad \text{and} \quad \left(\infty, r_2^S\right), \tag{15}$$

where the infinite values correspond to the principal directions aligned with the rulings, and the second values correspond to the directions perpendicular to the tool's axis. Therefore the (second) curvature radius of the tool ranges between

$$\left[r_1^S, r_2^S\right]. \tag{16}$$

Consider now the discrete set of hyperbolas $H_i$, $i = 1, \ldots, n$ and the corresponding set of the major semi-axes, $a_i$, $i = 1, \ldots, n$ and let us define its minimum as

$$\underline{a} = \min_{i=1,\ldots,n} a_i. \tag{17}$$

Observe that for an arbitrary (hyperbolic) point $\mathbf{q}$, $X$ can be always approximated by $T$ in second order line contact; the tool (its middle circle) just need to be sufficiently small. This is a fact that can be seen

in terms of Dupin indicatrices as follows: an arbitrary hyperbola can be in tangential contact with a pair of lines, if the lines have the freedom to move arbitrarily close one to another. This "arbitrarily close" corresponds to a sufficiently small radius of the tool.

Therefore, the condition that $T$ can access $X$ in second order line contact everywhere (up to the accuracy of the dicretization) is expressed by

$$\Omega_1 : \sqrt{\frac{r_1^S + r_2^S}{2}} \leq \underline{a}. \tag{18}$$

*4.2. Cutter selection*

We explore the three-parameter family of truncated cones and look for those whose helical motions can well approximate $X$. We want to restrict the search space as much as possible. In addition to (18), there are constraints on the triplet of parameters $(\alpha, r_1^c, r_2^c)$ that come from the specific geometry of the screw rotor as well as from the specific (helical) motion. The "valley" that needs to be machined has its upper and lower distance bound on the opposite faces.

We employ the method for double-flank milling of screw rotors using properly designed, custom-shaped, tools [8]. Such a custom-shaped tool, $T_{custom}$, corresponds to the maximal tool which can be placed into the rotor valley, see Fig. 5 (b). Hence we restrict our search space by conditions reflecting the constraints that the tool fits into that part of the valley:

$$r_1^c \leq c\, D_{min}, \quad \text{and} \quad r_2^c \leq c\, D_{max}, \tag{19}$$

where $D_{min}$ and $D_{max}$ correspond to the radii of the boundary circles of $T_{custom}$. The parameter $c$ controls the buffer around the tool, that gives some extra space that is used, e.g., for the coolant. This parameter is set to 0.9 in our implementation.

Another constraint that comes from the depth of the valley is the constraint on the length $h$ of the tool see Fig. 5 (b). Let $D_{depth}$ be the depth of the valley corresponding to the length of $T_{custom}$, then one obtains

$$\Omega_2 : D_{depth} \geq h = \frac{r_2^c - r_1^c}{\tan\alpha} \tag{20}$$

Finally, we constraint the opening angle of the tool by

$$\alpha \leq D_{angle} \tag{21}$$

and $D_{angle} = \pi/4$ in our implementation.

The constraints (19) and (21) define a cube in the $(\alpha, r_1^c, r_2^c)$-parameter space and two constraints (18) and (20) are two surfaces (plane $\Omega_1$ and curved surface $\Omega_2$) that further trim the cube, see Fig. 5 (c). Therefore, putting together the inequalities (18) - (21) we obtain a region in the $(\alpha, r_1^c, r_2^c)$-space of truncated cones that defines a domain of conical tools that can well approximate the given rotor geometry.

## 5. Flank milling of helical surfaces by conical tools

Let us assume now that both a helical surface $X$ (to be milled) and a conical tool $T$ are given. Due to the helical shape of $X$, it is natural to constraint the motion of $T$ as the corresponding helical motion. We therefore look only for the position of the axis $o$, i.e., for the values of $(\delta, \varrho, \beta, \phi)$, recall Fig. 2 (a) and the meaning of the parameters: $\delta$ and $\beta$ control the position of the (infinite) axis w.r.t. the helical axis $z$, $\phi$ controls the rotation around $z$, and $\varrho$ (together with the length $L$) determines the position of the finite axis.

*5.1. Initial positions computation*

To initialize the position of a cone for flank milling, we follow the initialization approach introduced in [25]. The linear meridian gives a simple constraint on the behavior of the distance function $d$ between points

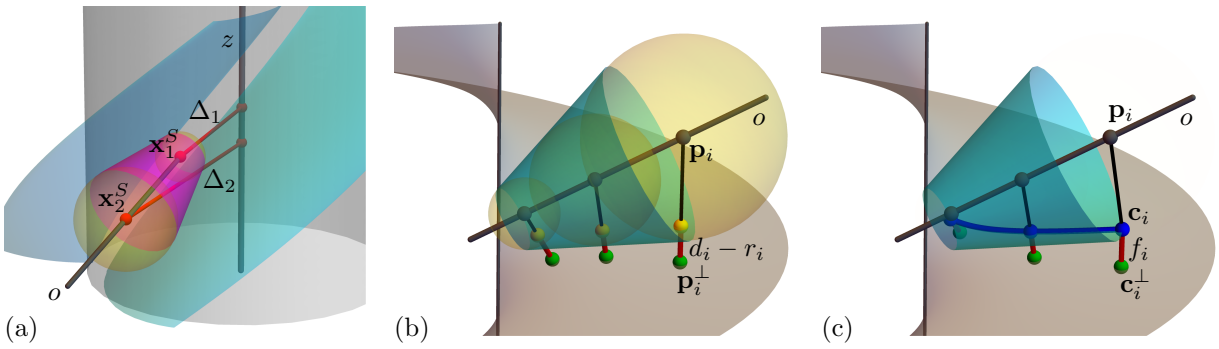


Figure 6: (a) Admissible orientation of the tool – the orientation of the tool satisfies the condition (24), which requires that the tool tip $\mathbf{x}_1^S$ is in the rotor cavity (closer to the $z$-axis) than the bottom point $\mathbf{x}_2^S$. (b) Optimization from Section 5.2 of the tool orientation minimizes the difference between the distances $d_i$ of the tool axis and the reference surface $X$ and radii $r_i$ of the tool $T$. (c) Optimization from Section 5.4 of the tool orientation minimizes the distances $f_i$ of the tool characteristic **ch** (w.r.t. the given helical motion) and the reference surface $X$.

in 3D and the reference surface $X$. Consider all 3D lines $\ell$ passing through a fixed point $\mathbf{p}$. One seeks unit directional vectors $\mathbf{v}$ of $\ell$ such that the second directional derivative of $d$ at $\mathbf{p}$ in a direction $\mathbf{v}$ vanishes, i.e.,

$$\nabla_{\mathbf{v}}(\nabla_{\mathbf{v}} d) = \nabla_{\mathbf{v}}^2 d = 0, \tag{22}$$

which corresponds to directions in which the distance function changes linearly as we move from $\mathbf{p}$ in the direction $\mathbf{v}$. Consequently it is a local constraint for an axis direction of a conical tool.

At a generic point $\mathbf{p}$, there are at most four directions $\mathbf{v}$ that satisfy (22) which give a multi-valued vector field of "good directions", see [25]. These directions correspond to positions of the conical axis such that the distance $d$ to $X$ changes linearly according to the linear slope of the radial function, which is a second order match. However, this matching is a good fit only locally, at a point of contact (the footpoint $\mathbf{p}^\perp$ of $\mathbf{p}$ on $X$) and one intends to get a good initial guess over a whole domain (corresponding to the length of the tool's axis). Therefore one integrates such multi-valued vector field to construct a family of integral curves, and, among them, linear segments are sought for. The segments extracted by [25] are not completely straight, but almost-straight up to some numerical tolerance, and therefore a straight line is fitted and the very end. Such a line then serves as our initial guess of a conical axis.

The axis, and the associated conical tool, should move tangentially to $X$, however, at the same time it should undergo the helical motion (defined by the rotor geometry). Therefore we use the known helical motion $S^{\pm}_{t,z,v_0}$, normalize the velocity vector at the midpoint of the axis, and compute

$$F(\ell) = \frac{1}{n}\sum_{i=1}^{n} \langle \mathbf{v}_i, \frac{\mathbf{p}_i - \mathbf{p}_i^\perp}{\|\mathbf{p}_i - \mathbf{p}_i^\perp\|} \rangle^2, \tag{23}$$

where $n$ is the number of sampled points $\mathbf{p}_i$ on $\ell$, $\mathbf{p}_i^\perp$ are their orthogonal projections onto $X$, and $\mathbf{v}_i$ are instantaneous velocities after the normalization ($\|\mathbf{v_m}\| = 1$). The value $F(\ell)$ is used as a tangential movability measure and lines $\ell$ with small values of $F$ are kept in the list, while those with large values are pruned away.

Note that a typical conical tool has a larger radius closer to the handler/shank and smaller radius closer to the tool tip. Due to the geometry of a screw rotor, this means that the tool tip should point towards that helical valley, and therefore be closer to the helical axis than the point closer to the shank, see Fig. 6 (a). Let $z$ be the helical axis, $\mathbf{x}_1^S$ and $\mathbf{x}_2^S$ be the boundary points on the tool axis $o$, and $r_1^S$ and $r_2^S$ be the corresponding candidate tool radii (the distances to the reference surface). To find admissible positions of the axis that point towards $z$, we simply test:

$$\Delta_1 = \mathrm{dist}(\mathbf{x}_1^S, z) < \mathrm{dist}(\mathbf{x}_2^S, z) = \Delta_2 \tag{24}$$

and if $r_1^S < r_2^S$, we keep the candidate line, otherwise we prune it away from our list.

*5.2. Optimization of the initial positions*

To further improve the tangential contact position between the tool and the surface, we optimize the position of the tool axis by minimizing the differences between the radial function $r(s)$ and distance $d(s)$ of $o$ and the target surface $X$. In particular, for a given position of the axis $o$ we compute the foot points $\mathbf{p}_i^\perp$ of the points $\mathbf{p}_i = \mathbf{o}(s_i)$, $s_i = i/(n-1)$, $i = 0, \ldots, n-1$, sampled on the axis $o$, see Fig. 6, (b). Then we define the objective function $\Phi_1$ as the sum of differences between $d_i = \|\mathbf{p}_i^\perp - \mathbf{p}_i\|$ and $r_i = r(s_i)$, where $r(s)$ is a prescribed radial function of a given tool, cf. (9)

$$\Phi_1(\delta, \varrho, \beta, \phi) = \sum_{i \in I_1} (d_i - r_i) + w \sum_{i \in I_2} (r_i - d_i)\,, \tag{25}$$

where $d_i \geq r_i$ for $i \in I_1$ and $d_i < r_i$ for $i \in I_2$. Minimizing $\Phi_1$ yields the values $(\delta, \varrho, \beta, \phi)$, determining the optimized position of the tool $T$. Finally, by applying a screw motion on $T$ we obtain its flank milling path.

**Remark 5.1.** To penalize the parts with the over-cutting index set ($I_2$) we set the weight $w = 100$. In all our examples we choose the number of samples $n = 100$ as a suitable compromise between accuracy and speed of computation. For minimizing $\Phi_1$ we employ the gradient descent method, where the gradient is approximated using the finite differences. As a termination criterion, we check the two subsequent values in the optimization process, and if they do not differ by more than a prescribed value, i.e., $\|\mathbf{x}_{i+1} - \mathbf{x}_i\| < \varepsilon = 10^{-5}$, we stop the optimization.

One could eventually use more advanced optimization techniques than gradient descent, e.g. the Levenberg-Marquardt algorithm, however, the impact of a good initial guess, in our case constructed as described in Section 5.1, turned out to be more important than the particular optimization method in similar problems [26].

The designed method yields a position of the conical tool $T$ (its axis $o$) and an array $\{d_i\}_{i=0}^{n-1}$ describing the distances of $o$ and $X$, i.e.,

$$d_i = \|\mathbf{p}_i^\perp - \mathbf{p}_i\| \qquad i = 0, \ldots, n-1, \tag{26}$$

such that $\sum |r_i - d_i|$ is minimal. The error of the approximate flank machining (along the axis $o$ of $T$) is measured as the distances between $T$ and $X$ which corresponds to

$$e_i = d_i - r_i. \tag{27}$$

Since the tool is moved in the same helical motion as the profile curve (and the characteristic) error function (27) (along $o$) remains exactly the same as the tool moves in time.

*5.3. Optimization of the tool and its initial positions*

Employing small modifications of the optimization approach from Section 5.2, we can simultaneously look for the optimal conical tool and its initial positions. In particular, we optimize the tool axis that minimizes the tool-surface error and simultaneously provide a linear radial function.

More precisely, for a given position of the axis $o$ we compute the foot points $\mathbf{p}_i^\perp$ of $\mathbf{p}_i = \mathbf{o}(s_i)$, uniformly sampled on the axis $o$ and construct the objective function $\Phi_2$ demanding $d_i = \|\mathbf{p}_i^\perp - \mathbf{p}_i\|$ to be as linear as possible:

$$\Phi_2(\delta, \varrho, \beta, \phi) = \sum_{i=0}^{n-1} d_{i+2} - 2d_{i+1} + d_i. \tag{28}$$

Minimizing $\Phi_2$ yields the values $(\delta, \varrho, \beta, \phi)$, determining the optimized position and the "almost" conical shape of the tool $T$. Since distances $d_i$ are not distributed exactly linearly we fit $d_i$ by a linear function $r(s)$ in the least squares sense, i.e.,

$$\sum_{i=0}^{n-1} |d_i - r(s_i)| \to \min\,. \tag{29}$$

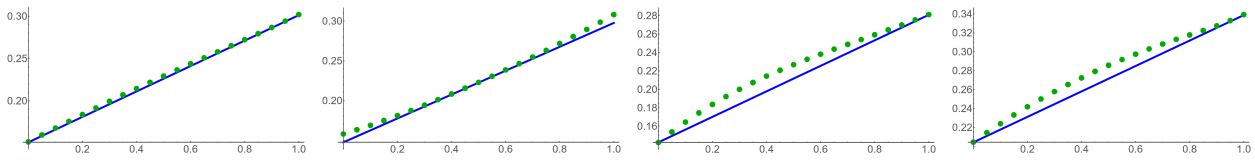

Figure 7: Fitting of the distances $d_i$ (green dots) by a linear function $r(s)$ (blue line) corresponding to the non-overcutting positions of the tool axis w.r.t. (from left to right) surfaces $X_1$ and $X_2$ of the male rotor and $X_1$ and $X_2$ of the female rotor from Example 6.1.

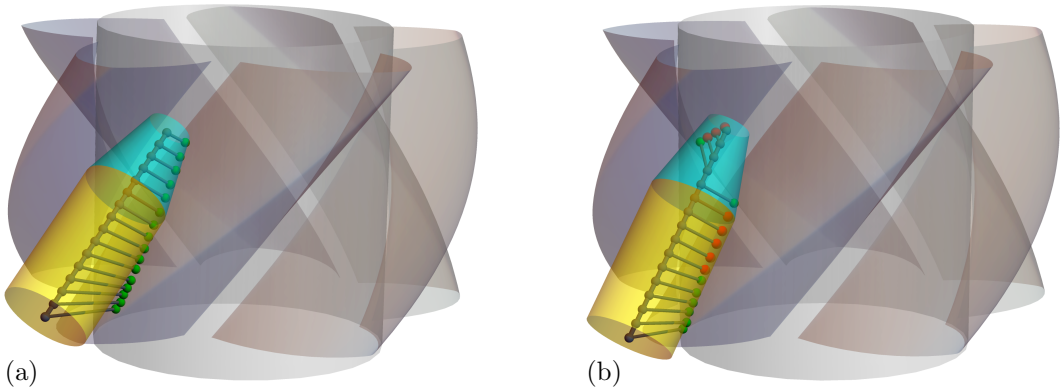


Figure 8: Global collision test. Footpoints passing the distance check (green) and those that fail (red) are shown. When all points pass the check (a), the position is marked as non-colliding. If at least one point fails the check, the position is marked as colliding (b) and is eliminated from the list.

In our implementation of the least squares method, we also employ the constraints

$$d_i \geq r(s_i), \quad i = 0, \ldots, n-1, \tag{30}$$

which reflects our wish that the tool is globally non-overcutting, see Fig. 7. Again, the final step is to apply a screw motion on $T$ which gives the sought-after flank milling path.

### *5.4. Optimization of the initial positions based on velocity motion*

The optimization technique described in section 5.2 is independent of the specific helical motion – it only minimizes the distance between the tool and the reference surface. In addition, it can also be adapted to design an optimal conical tool by making minor modifications, see Section 5.3.

In this section, however, we introduce another optimization method that incorporates directly the specific (and given) helical motion. Specifically, we minimize the distance between the tool characteristic (with respect to the prescribed helical motion) and the helical surface. The advantage of incorporating the helical motion into the optimization is faster convergence to the minimum.

Let us discuss the approach in more detail, for a given position of the axis $o$, helical motion (given by $z$ axis and value of the pitch $2\pi v_0$) and radial function $r(s)$, cf. (9), we compute the characteristic $\mathbf{ch}(s)$ (11). Now sampling the axis $\mathbf{p}_i = \mathbf{o}(s_i)$, characteristic $\mathbf{c}_i = \mathbf{ch}(s_i)$, $s_i = i/(n-1)$, $i = 0, \ldots, n-1$, and computing the corresponding foot points $\mathbf{c}_i^{\perp} \in X$ we define the objective function $\Phi_3$ as the sum of distances $f_i = \|\mathbf{c}_i^{\perp} - \mathbf{c}_i\|$, recall Fig. 6 (c)

$$\Phi_3(\delta, \varrho, \beta, \phi) = \sum_{i \in I_1} f_i + w \sum_{i \in I_2} f_i. \tag{31}$$

Analogously as in Section 5.2, $\|\mathbf{p}_i - \mathbf{c}_i^{\perp}\| \geq \|\mathbf{p}_i - \mathbf{c}_i\|$ for $i \in I_1$ and $\|\mathbf{p}_i - \mathbf{c}_i^{\perp}\| < \|\mathbf{p}_i - \mathbf{c}_i\|$ for $i \in I_2$.

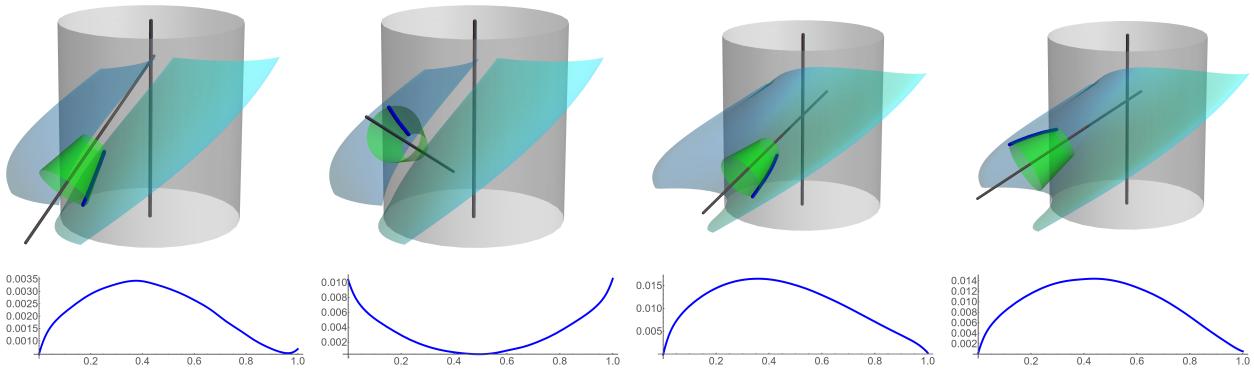

Figure 9: Top: Particular positions of four different optimized conical tools on (from left to right) surfaces $X_1$ and $X_2$ of the male rotor and $X_1$ and $X_2$ of the female rotor from Example 6.1. The optimized linear radial functions are shown in Eqns. (32) and (33). Bottom: The corresponding error functions (27) (along the axis $o$).

**Remark 5.2.** In our tests, see Section 6, the optimization techniques described in Sections 5.2 and 5.4 provide comparable results in terms of the accuracy of the final tool orientation relative to the target geometry. However, the method described in this section (based on a specific helical motion) generally converges to the minimum faster, and therefore fewer iterations are needed to achieve a fine machining tolerance.

*5.5. Global collision detection*

To return physically feasible paths, one has to consider also the global collision of the cutter $T$ with the whole object $O$, not just the flank surface $X$. The analysis described in the previous sections takes care of local collisions. To control global collisions, we perform a simple collision test as follows. The cutting part of the tool is conceptualized as a truncated cone $T$ while the *shank* is represented as a cylinder, see Fig. 8. The real shank is a more complex object, so similarly to [24], its cylindrical bound is taken for the sake of simplicity in our collision test.

Either the tool or the shank can collide with $O$ globally. To detect a collision of $T$, we sample the axis $o$ and compute the footpoints on $O$. For a sample point $\mathbf{p}_i$, the projection algorithm returns its footpoint $\mathbf{p}_i^{\perp}$, see Fig. 8, and we perform a distance check $\|\mathbf{p}_i - \mathbf{p}_i^{\perp}\| < r_i$, $r_i$ being the corresponding radius of the inscribed sphere that corresponds to the position $\mathbf{p}_i$. For the cylindrical shank, we proceed analogously with the difference of the constant (cylindrical) radius. If the collision is realized at some point, the collision routine is terminated, and the corresponding position of the tool is labeled as colliding.

## 6. Examples

In this section, we present several examples of how our algorithms perform on industrial benchmarks – namely on all helical surfaces of the screw rotor with the 'N' profile (Stosic, 1996). The screw rotors geometries have mostly non-symmetric profiles which makes them difficult to get machined using double-flank machining with custom-shaped tool [8]. For these geometries, each flank has to be machined separately, and our approach looks for fine approximation by a few sweeps of a single conical tool.

**Example 6.1** (One sweep – tool optimization)**.** We start with the initial tool with $\alpha = 0.25, r_1^c = 0.25, r_2^c = 0.5$. We demonstrate the computation of particular optimal tool's radial functions (Section 5.3) and positions for each of the helical surfaces $X_1$ and $X_2$ (two parts of each rotor) of the well-known male and female screw rotors with asymmetric 'N' profiles.

In the case of the male rotor, we end up with the tools having the radial functions described by

$$r_1(s) = 0.150s + 0.149, \quad \text{and} \quad r_2(s) = 0.150s + 0.151, \quad s \in [0, 1] \tag{32}$$

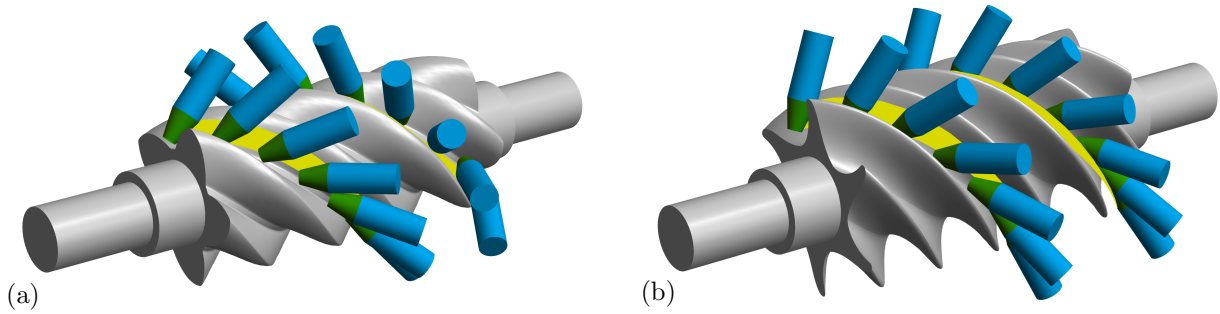


Figure 10: Globally collision-free flank milling of the male (a) and female (b) screw rotors with the asymmetric profiles ('N' profile, Stosic, 1996) from Example 6.1. On each rotor, we use two different conical tools and visualize the motion by several positions, including the shank (blue cylinders), to demonstrate the collision-free motion.

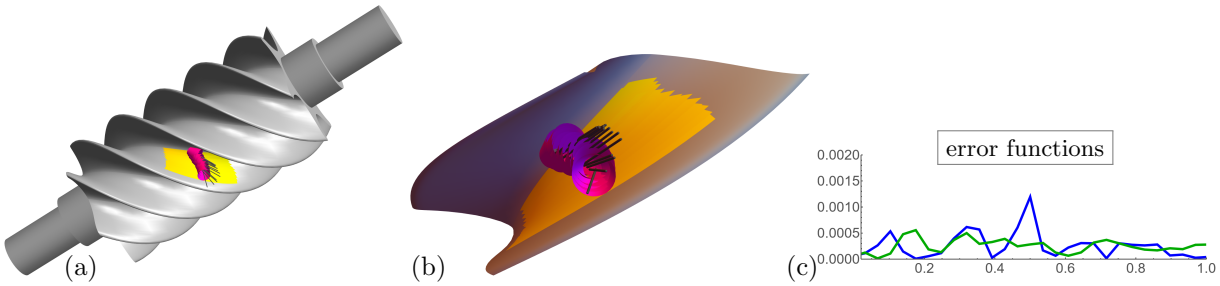


Figure 11: Approximation of the first helical surface of the screw rotor ('N' profile, Stosic, 1996) from Example 6.2. (a) 15 optimized positions of a single conical tool (magenta) and the corresponding envelope strips (yellow). (b) A zoom in of the helical flank and the envelopes. (c) The approximation errors using optimization from Sections 5.2 (blue) and 5.4 (green) between the envelopes and the helical surface measured along a profile curve.

for surfaces $X_1$ and $X_2$, respectively, see Fig 7. For female rotor we obtained

$$r_1(s) = 0.138s + 0.143, \quad \text{and} \quad r_2(s) = 0.134s + 0.205, \quad s \in [0, 1]. \tag{33}$$

The tools and their particular positions are shown in Figs. 9 and 10. The maximal distances between the tool and the surfaces $X_1$ and $X_2$ of the male rotor are less than 0.00346 and 0.01051, respectively. For the female rotor we obtain 0.01653 and 0.01446. These values are relative to the radius $R = 1$ of the cylindrical body of both rotors.

The approximation errors in Example 6.1 do not meet the machining tolerances yet, but these errors are coming from a single sweep of the tool and can be significantly reduced by using multiple milling paths.

**Example 6.2** (More sweeps – female rotor $X_1$)**.** When using only one envelope strip with a tool from Example 6.1 to the helical surface $X_1$ of the female rotor, we obtained the maximal error equal to 0.01653. To reduce this error, we employ smaller tool and perform machining simulations with several strips. In this experiment, we set $\alpha = \sin(0.3), r_1^c = 0.1, r_2^c = 0.18$.

We start with 18 different initial positions initialized by the approach described in Section 5.1, using uniformly sampled points along the profile curve. We optimize the position and impose two constraints: (1) the distance of the tool (in the optimized position) can not be larger that error threshold $\varepsilon = 0.002$. (2) the tool (including the shank) cannot penetrate the screw rotor. That is, each cone is globally collsion-free with both sides of the helical cavity. We employed the two optimization methods from Sections 5.2 and 5.4. In both cases conditions (1) and (2) were satisfied by 15 optimized tool positions, see Fig. 11 (a). The whole error behavior along a profile curve based on minimizing $\Phi_1$ (resp. $\Phi_3$) is shown in blue (resp. green) in Fig. 11 (c).

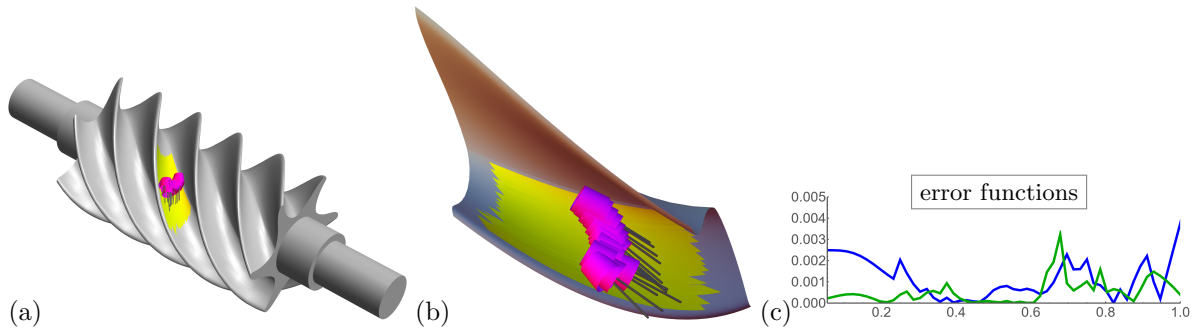


Figure 12: Approximation of the second helical surface of the screw rotor ('N' profile, Stosic, 1996) from Example 6.3. (a) 14 out of 18 optimized positions met the requirements. (b) A zoom in of the flank and the envelopes. (c) The approximation errors using optimization from Sections 5.2 (blue) and 5.4 (green) between the envelopes and the helical surface measured along a profile curve.

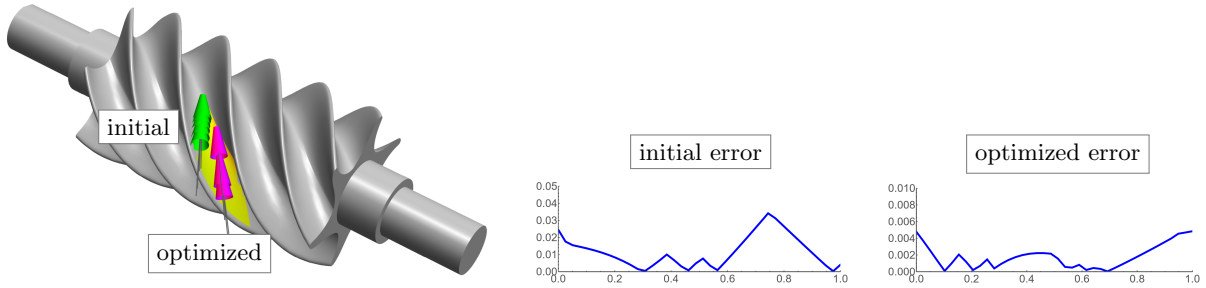


Figure 13: Approximate flank milling of the helical surface $X_2$ on the female screw rotors ('N' profile, Stosic, 1996) from Example 6.4.

**Example 6.3** (More sweeps – female rotor $X_2$)**.** When using only one envelope strip with a tool from Example 6.1 to the helical surface $X_2$ of the female rotor, we obtained the maximal error equal to 0.01446. To reduce this error, we employ smaller tool and apply our path-planning algorithm with several strips. In this test we set $\alpha = \sin(0.1), r_1^c = 0.129, r_2^c = 0.18$, and we set the error threshold to 0.004.

We started with 18 initial positions sampled uniformly along the profile curve. We optimized the positions, prescribing the same two constraints as in Example 6.2.

We again employed the two optimization methods from Sections 5.2 and 5.4. In both cases conditions were satisfied by 14 optimized tool positions, see Fig. 12 (a). All positions of the axis are globally collision-free with the whole rotor geometry and meet the error threshold, see Fig. 12 (c), for the error functions.

**Example 6.4** (Larger tool – female rotor $X_2$)**.** Another experiment we run is the machining of the helical surface $X_2$ of the female rotor ('N' profile, Stosic, 1996) with a large conical tool. Here we employed the tool with $\alpha = \sin(0.2), r_1^c = 0.07, r_2^c = 0.2$ and used path-planning algorithm from Section 5.2. The error threshold was set to 0.01. We started with 6 initial positions and after optimization and collision tests we ended up with three optimized positions of the tool, see Fig. 13.

**Example 6.5** (More sweeps – male rotor $X_1$)**.** When using only one envelope strip with a tool from Example 6.1 to the helical surface $X_1$ of the male rotor we obtained the maximal error equal to 0.00346. Now, we employ a smaller tool and apply our path-planning algorithm from Section 5.2 with several strips. In this test we set $\alpha = \sin(0.1), r_1^c = 0.12, r_2^c = 0.14$, and we set the error threshold to 0.003.

We started with 12 initial positions sampled uniformly along the profile curve. We optimized the positions, prescribing the same two constraints as in Example 6.2. The conditions were satisfied by 7 optimized

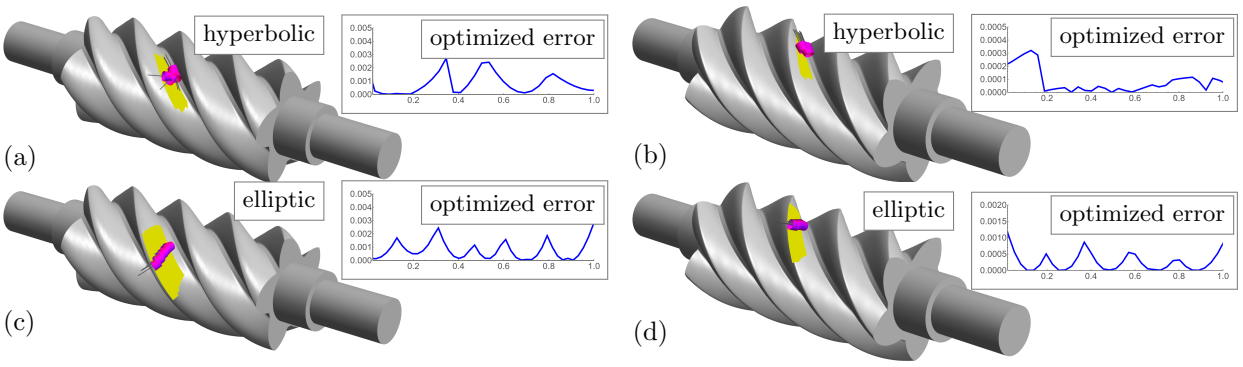


Figure 14: Approximation of helical surfaces $X_1$ (a,c) and $X_2$ (b,d) of the male screw rotor ('N' profile, Stosic, 1996) from Example 6.5. (a,b) The approximation of the hyperbolic part. 7 out of 12 optimized positions met the requirements (a). All 11 optimized positions met the requirements (b). (c,d) The approximation of the elliptic part, where we employed the initialization using the tangential contact. 7 out of 12 optimized positions met the requirements (c) and 5 out of 6 optimized positions met the requirements (d). The approximation errors between the envelopes and the helical surface measured along a profile curve are also shown.

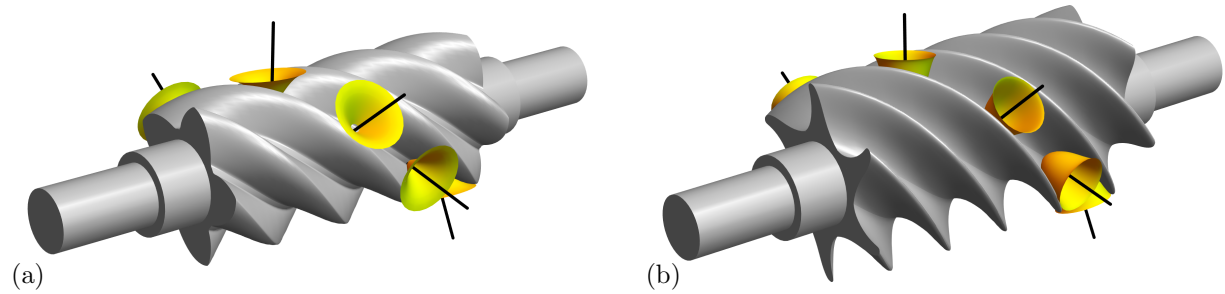


Figure 15: Approximate double-flank milling of male (a) and female (b) screw rotors with asymmetric profiles ('N' profile, Stosic, 1996) with custom-shaped tool [8]. Several positions of two custom-shaped tools are shown.

tool positions, see Fig. 14 (a). The optimized positions are collision-free with the whole rotor geometry and meet the error threshold, see Fig. 14 (a-framed) also for the error function.

In the elliptic part, one cannot achieve higher than first order contact hence we align the axis of the tool with the principal direction that corresponds to the minimal curvature as this minimizes the error of the tangential contact, see Fig. 14 (c).

**Example 6.6** (More sweeps – male rotor $X_2$)**.** When using only one envelope strip with a tool from Example 6.1 to the helical surface $X_2$ of the male rotor we obtained the maximal error equal to 0.01051. To reduce this error, we employ smaller tool and apply our path-planning algorithm from Section 5.2 with several strips. In this test we set $\alpha = \sin(0.1), r_1^c = 0.11, r_2^c = 0.13$, and we set the error threshold to 0.002.

We started with 11 initial positions sampled uniformly along the profile curve and again optimized the positions under the same two constraints as in Example 6.2. The conditions were satisfied by all 11 optimized tool positions, see Fig. 14 (b). The optimized positions are collision-free with the whole rotor geometry and meet the error threshold, see Fig. 14 (b-framed) also for the error function. In the elliptic part, one can aim only at the first order contact and we again aligned the axis of the tool with the principal direction that corresponds to the minimal curvature. The results are shown in Fig. 14 (d).

**Example 6.7** (Comparison against double-flank milling using custom-shaped tools)**.** We compare the method for flank milling of screw rotors by conical tools from Section 5.2 with approach presented in [8], where the entire helical valley of the rotor is approximated by a single sweep of a custom-shaped tool. That approach uses only one sweep, however, it requires a special, custom-shaped, tool, see Fig. 15. In

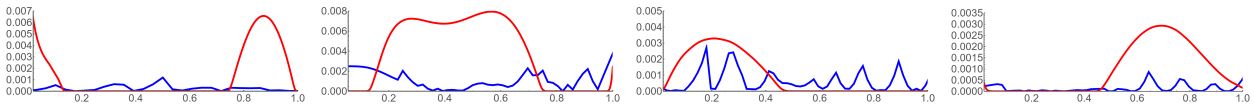

Figure 16: Conical vs. custom-shaped. A comparison of the errors using flank milling by conical tools (blue) and double-flank milling using a custom-shaped tool (red) [8], tested on the asymmetric screw rotor ('N' profile, Stosic, 1996). Four helical surfaces were tested: surfaces $X_1$ and $X_2$ of the male rotor and $X_1$ and $X_2$ of the female rotor (from left to right).

| Example | # vertices | diam | $e_{max}$ | time-ini | time-opt |
|---|---|---|---|---|---|
| Fig. 10 female $X_1$ | 16K | 6.25 | 0.00437 | 2.2s | 0.73s |
| Fig. 10 female $X_2$ | 14K | 6.25 | 0.01128 | 2.1s | 0.82s |
| Fig. 10 male $X_1$ | 17K | 6.25 | 0.01689 | 3.4s | 1.17s |
| Fig. 10 male $X_2$ | 16K | 6.25 | 0.01070 | 2.8s | 0.45s |
| Fig. 11 female $X_1$ | 16K | 6.25 | 0.00143 | 410s | 24.34s |
| Fig. 12 female $X_2$ | 14K | 6.25 | 0.00357 | 220s | 22.06s |
| Fig. 13 female $X_2$ | 16K | 6.25 | 0.00489 | 1010s | 11.01s |
| Fig. 14 male $X_1$ | 17K | 6.25 | 0.00294 | 45s | 24.14s |
| Fig. 14 male $X_2$ | 16K | 6.25 | 0.00136 | 85s | 18.52s |

Table 1: The statistics of our algorithm. In turn, we report the number of the mesh vertices ($X_1 \cup X_2$), the diameter of the bounding box of the whole rotor, the maximum error, and the computation time (in secs) of the initialization and optimization stages.

contrast, our approach uses a standard conical tool and, with the option of several milling paths, overall provides a better approximation, see Fig. 16.

The initialization stage (Section 5.1) was implemented in C++ language and ran on a desktop with CPU i7-10700K 3.80 GHz and 16G RAM. The optimization stage ( Sections 5.2, 5.3 and 5.4) was implemented in Mathematica and ran on a desktop with CPU i7-10510U 2.30 GHz and 16G RAM. The statistics of our algorithm on all the rotor examples shown in the paper are listed in Table 1.

### *6.1. Discussion & limitations*

*General helical surfaces.* Recently, a method for double-flank milling of helical rotors has been introduced in [8]. Therefore, we demonstrate our general approach on the case of helical rotors, since we can compare the method with the method from [8]. However, the presented approach can be directly applied to any helical surface.

*Elliptical parts.* The proposed approach focuses on the use of conical tools and for the elliptical parts of the screw rotors, recall Fig. 3, one cannot achieve higher than first order contact. Therefore, our initialization strategy proposed in Section 5.1 cannot find any good positions (as it aims at higher order of contact). In these parts, one has no better option but to use any tangential configuration [13].

*Global collision.* In our implementation, the global collision is tested as a post-process, i.e., the computed tools' positions are tested at the very end of our algorithm and the colliding positions are filtered out. Conceptually a better solution would incorporate the collision avoidance as a part of the optimization algorithm. However, such an approach would require a special datastructure for fast computation of the footpoints, see e.g. [27, 28], and also an efficient approximation of the point-surface distance, which goes beyond the scope of this paper.

*Gaps between strips.* The samples on the profile curve were selected sufficiently dense to end up with a solution that does not contain gaps between neighboring strips. One could derive a bound on such a sampling density based on the curvature of the tool and the rotor, however, such a bound would very likely require excessive number of positions. Another point is that we sampled the contact points uniformly along the profile curve, which led to lower errors in some parts and larger errors in the others. An alternative strategy would be to start with a coarse set of sampling points and insert adaptively new samples in places where the approximation error is the worst. This could eventually reduce the number of the milling paths.

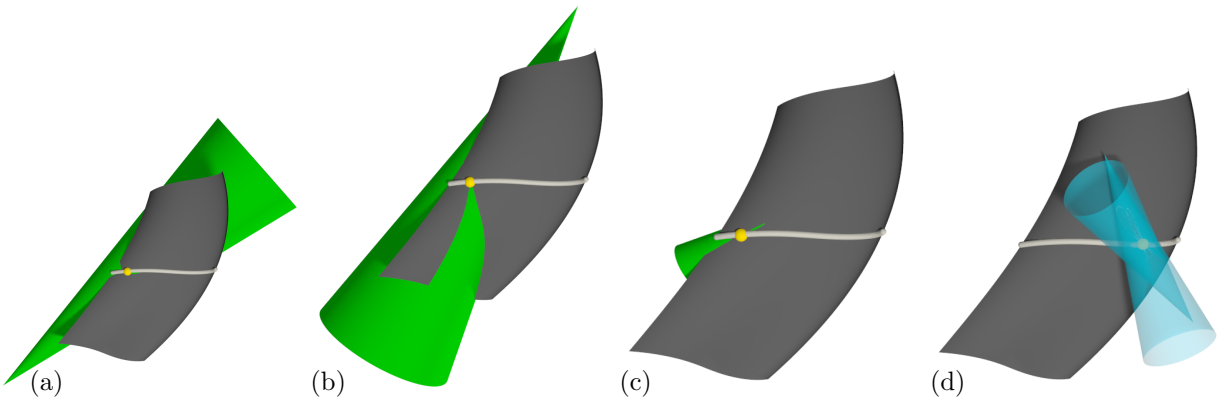


Figure 17: Hyperosculation. For a fixed cone of the opening angle of 10°, the hyperosculating cones [29] are computed. The view is upside down, i.e., we look at the rotor flank from the material side. While at some points (yellow) of the profile curve (light grey) there are hyperosculating cones (green) on the machining side (a-c), at some points (d), there exist hyperosculating positions (transparent) only on the material side.

*Custom-shaped vs. on-market tools.* Results shown in Fig. 16 bring a qualitative comparison between the use of a single sweep of a custom-shaped tool vs. several paths of a given (on-market) conical tool. One can use these results for consideration of the trade-off between the machining time (higher for conical tools) and the manufacturing cost (higher for custom-shaped tools).

*Initialiazation using hyperosculating cones.* We also experimented with the initialization using hyperosculating (3rd order contact in the isotropic model of the Laguerre geometry) positions of a given conical tool and the reference surface [29], see Fig. 17. In general, there exist up to 6 real hyperosculating cones at a given point of contact. However, the distance between the cone's vertex and the contact point may vary throughout the surface. This fact makes the selection of the tool problematic as one needs to find a range for the vertex-contact point distance such that there is a hyperosculating position for every (sample) point on the profile curve. Moreover, there might be points where all the hyperosculating cones appear only on the material side, see Fig. 17(d), therefore being useless for our CNC machining application. One would need to look also for a suitable opening angle of the cone, which goes beyond the current paper.

## 7. Conclusion

A new path-planning algorithm for 5-axis flank CNC machining of screw rotors has been proposed. For a given conical tool, the search for good initial positions is accomplished by looking at second order contact of the rotor geometry and the tool. The initialization stage returns a set of discrete tool positions that consequently undergo a global optimization that further reduces the error between the tool and the rotor geometry.

In the case of no given conical tool, we look for the best tools' shape by considering a linear radial function and by optimizing the tool axis that minimizes the tool-surface error, and the tool-surface engagement is non-overcutting. The proposed algorithm has been validated on several benchmark industrial datasets, demonstrating to meet fine machining tolerances with only a few sweeps of a conical tool.

As a future research, we aim at physical validations of the proposed path-planning algorithm. Another future research direction is that the current solution is a union of milling paths that overlap. Even though the approximation errors are under a given threshold, this overlapping can introduce artifacts in the real machining. Therefore, we aim to look at milling paths such that the neighboring envelops are non-overlapping and joined in a $G^1$ fashion.

## Acknowledgment

This work was supported by the Spanish Ministry of Science, Innovation and Universities, grant No PID2019-104488RB-I00, BCAM "Severo Ochoa" accreditation (SEV-2017-0718), and by the European Union's Horizon 2020 program under grant agreement No 862025. Michael Bartoň was supported by the Ramón y Cajal fellowship RYC-2017-22649. Michal Bizzarri was partially funded the Czech Ministry of Education, Youth and Sports and Pengbo Bo was supported by the National Natural Science Foundation of China (Grant No. 62072139). We would also like to thank an anonymous reviewer for the alternative optimization idea presented in Section 5.4.

## References

[1] B. K. Choi, R. B. Jerard, Sculptured Surface Machining: Theory and Applications, Kluwer, 1998.
[2] J. Wallner, G. Glaeser, H. Pottmann, Geometric contributions to 3-axis milling of sculptured surfaces, in: [? ], 1999, pp. 33–41.
URL http://www.geometrie.tugraz.at/wallner/impossible.pdf
[3] J. Wallner, H. Pottmann, On the geometry of sculptured surface machining, in: P.-J. Laurent, P. Sablonnière, L. L. Schumaker (Eds.), Curve and Surface Design: Saint Malo 1999, Vanderbilt University Press, Nashville, 2000, pp. 417–432.
URL http://dmg.tuwien.ac.at/geom/ig/papers/pot105.zip
[4] D. Roth, S. Bedi, F. Ismail, S. Mann, Surface swept by a toroidal cutter during 5-axis machining, Computer-Aided Design 33 (1) (2001) 57–63.
[5] C. G. Jensen, W. E. Red, C. Ernst, Machining free-form surface cavities using a combination of traditional and non-traditional multi-axis machining methods, Computer-Aided Design & Applications 5 (2008) 241–253.
[6] D. He, Z. Li, Y. Li, K. Tang, Quasi-developable and signed multi-strip approximation of a freeform surface mesh for efficient flank milling, Computer-Aided Design 140 (2021) 103083.
[7] W. Gao, Y. Zhang, D. Ramanujan, K. Ramani, Y. Chen, C. B. Williams, C. C. Wang, Y. C. Shin, S. Zhang, P. D. Zavattieri, The status, challenges, and future of additive manufacturing in engineering, Computer-Aided Design 69 (2015) 65–89.
[8] M. Bizzarri, M. Bartoň, Manufacturing of screw rotors via 5-axis double-flank CNC machining, Computer-Aided Design 132 (2021) 102962.
[9] A. Kovacevic, N. Stosic, I. K. Smith, Advanced methods and tools for screw compressor design, Proceedings of the TMCE 2006.
[10] N. Stosic, I. K. Smith, A. Kovacevic, E. Mujic, Geometry of screw compressor rotors and their tools, Journal of Zhejiang University-SCIENCE A 12 (4) (2011) 310–326.
[11] L. Rinder, Screw rotor profile and method for generating, US Patent 4,643,654 (1987).
[12] N. Stosic, I. Smith, A. Kovacevic, Rotor interference as a criterion for screw compressor design, Journal of Engineering Design 14 (2) (2003) 209–220.
[13] W. Wunderlich, Geometrische Grundlagen für das Fräsen von Schraubnuten I, Österr. Ing.-Archiv 6 (1952) 315–326.
[14] F. L. Litvin, P.-H. Feng, Computerized design, generation, and simulation of meshing of rotors of screw compressor, Mechanism and Machine Theory 32 (2) (1997) 137–160.
[15] J. Machchhar, H. Segerman, G. Elber, Conjugate shape simplification via precise algebraic planar sweeps toward gear design, Computers & Graphics 90 (2020) 1–10.
[16] F. L. Litvin, A. Fuentes, Gear geometry and applied theory, Cambridge University Press, 2004.
[17] Y.-R. Wu, Z.-H. Fong, Optimization design of an explicitly defined rack for the generation of rotors for twin-screw compressors, Mechanism and Machine Theory 44 (1) (2009) 66–82.
[18] D. Zaytsev, C. I. Ferreira, Profile generation method for twin screw compressor rotors based on the meshing line, International Journal of Refrigeration 28 (5) (2005) 744–755.
[19] N. Stosic, E. Mujic, I. K. Smith, A. Kovacevic, Profiling of screw compressor rotors by use of direct digital simulation, International Compressor Engineering Conference (2008) 1860.
[20] J. Do Suh, D. G. Lee, Manufacture of composite screw rotors for air compressors by RTM process, Journal of Materials Processing Technology 113 (1-3) (2001) 196–201.
[21] N. Stosic, I. K. Smith, A. Kovacevic, Optimisation of screw compressors, Applied Thermal Engineering 23 (10) (2003) 1177–1195.
[22] H. Pottmann, M. Peternell, Envelopes-computational theory and applications, in: Proceedings of Spring Conference on Computer Graphics, 2000, pp. 3–23.
[23] M. Bizzarri, M. Lávička, J. Kosinka, Skinning and blending with rational envelope surfaces, Computer-Aided Design 87 (2017) 41–51.
[24] M. Bartoň, M. Bizzarri, F. Rist, O. Sliusarenko, H. Pottmann, Geometry and tool motion planning for curvature adapted CNC machining, ACM Trans. Graph. 40 (4) (2021) 180.
[25] P. Bo, M. Bartoň, H. Pottmann, Automatic fitting of conical envelopes to free-form surfaces for flank CNC machining, Computer-Aided Design 91 (2017) 84–94.
[26] P. Bo, M. Bartoň, On initialization of milling paths for 5-axis flank CNC machining of free-form surfaces with general milling tools, Computer Aided Geometric Design 71 (2019) 30–42.

[27] J.-W. Chang, W. Wang, M.-S. Kim, Efficient collision detection using a dual obb-sphere bounding volume hierarchy, Computer-Aided Design 42 (1) (2010) 50–57.
[28] S. Redon, M. C. Lin, D. Manocha, Y. J. Kim, Fast continuous collision detection for articulated models, Journal of Computing and Information Science in Engineering 5 (2) (2005) 126–137.
[29] M. Skopenkov, P. Bo, M. Bartoň, H. Pottmann, Characterizing envelopes of moving rotational cones and applications in CNC machining, Computer Aided Geometric Design 83 (2020) 101944.